

Hydrodynamic synchronization of spontaneously beating filaments

Brato Chakrabarti and David Saintillan*

Department of Mechanical and Aerospace Engineering,
University of California San Diego, 9500 Gilman Drive, La Jolla, CA 92093, USA
(Dated: April 24, 2019)

Using a sliding control model of the flagellar axoneme accounting for dynein motor kinetics, we study elastohydrodynamic phase synchronization in a pair of spontaneously beating filaments with waveforms ranging from sperm to cilia and *Chlamydomonas*. Our computations reveal that both in-phase and anti-phase synchrony can emerge for asymmetric beats while sperms always go in-phase, and elucidate the mechanism for phase slips due to biochemical noise. Model predictions agree with recent experiments and illuminate the crucial roles of hydrodynamics and mechanochemical feedback in synchronization.

Studies on the synchronization of biological oscillators date back to observations by Rothschild [1] on nearby swimming sperms and subsequent theoretical work by Taylor [2], who proved that dissipation for two swimming sheets is minimized for an in-phase configuration. While biology is often not driven by dissipation principles, it has long been hypothesized that fluid-mediated hydrodynamic interactions play a central role in synchronization and in collective behaviors such as metachronal waves in ciliary arrays [3]. Over the last two decades, experiments [4–9] using micropipette-held *Chlamydomonas* have revealed that elastohydrodynamic interactions may indeed be at play in causing its two flagella to synchronize their breaststrokes. Periods of asynchrony are thought to arise due to biochemical noise and are well described by a stochastic Adler equation [9, 10].

Theoretical progress in understanding synchronization is complicated by the intricate internal structure and actuation of the flagellum core, known as the axoneme. In presence of ATP, thousands of dynein molecular motors act in concert to bend the structure and drive spontaneous beats. Much work has gone into developing minimal models that neglect this biological complexity and coarse-grain flagella as microspheres driven on compliant or tilted orbits [11–14]. More detailed numerical models have relied on pre-imposed internal or external actuations to analyze metachronal waves [15, 16] or the bistability of elastic filaments [17], yet these descriptions poorly capture experimental waveforms. Only recently have there been attempts to study the role of hydrodynamics in simplified models of active elastic filaments [18].

While the detailed process leading to spontaneous flagellar oscillations remains controversial, several mechanisms have been proposed ranging from flutter-like instabilities [19–21] to dynamic internal tension [22] and geometric control of dynein kinetics [23–27]. Building on previous sliding control models [27, 28], we recently developed [29] a microscopic bottom-up description for an active elastic flagellum accounting for internal dynein motor kinetics, which produces spontaneous oscillations following saturation of a Hopf bifurcation and can generate a variety of beating patterns observed in nature. In

this Letter, this microscopic model is employed to analyze the temporal dynamics and synchronization of a pair of spontaneously beating filaments. Our results are consistent with recent experiments [9] and elucidate the crucial roles of hydrodynamic interactions, mechanochemical feedback, and biochemical noise in the process of synchronization.

Model formulation.—The flagellar axoneme is a 3D structure with circular cross-section composed of 9 pairs of microtubules arranged in a systematic cyclic fashion. Following past models [27, 29, 30], we idealize this structure as a planar projection with diameter a and length L , where microtubules are represented by two polar filaments \mathbf{x}_{\pm} clamped at the base [Fig. 1(a)]. We seek an evolution equation for the centerline $\mathbf{x}(s, t)$ parametrized by arclength $s \in [0, L]$. Internal actuation arises from dynein motors that extend from each filament and stochastically bind with the opposite one. In presence of ATP, these motors move along the filaments and generate internal shear forces resulting in an arc-length mismatch known as the sliding displacement [30]: $\Delta(s, t) = \int_0^s (|\partial_{s'} \mathbf{x}_-| - |\partial_{s'} \mathbf{x}_+|) ds' = a\phi(s, t)$, where $\phi(s, t)$ is the tangent angle. This sliding is resisted by internal protein linkers, or nexin links, modeled as linear springs of stiffness K . Both dynein motors and nexin links result in equal and opposite force densities along the filaments:

$$f_m(s, t) = \rho(n_+ F_+ + n_- F_-) - K\Delta, \quad (1)$$

where ρ is the mean motor density, n_{\pm} are the fractions of motors in the bound state, and F_{\pm} are the associated loads. These sliding forces generate internal moments $M(s, t) = B\phi_s - a \int_s^L f_m(s', t) ds'$, where the first term captures the passive elastic response of the structure modeled as an inextensible Euler-Bernoulli elastica with bending rigidity B [31]. Dynein motor populations evolve as $\partial_t n_{\pm} = \pi_{\pm} - \epsilon_{\pm}$ where π_{\pm} and ϵ_{\pm} are the attachment and detachment rates, respectively. The attachment rate is proportional to the fraction of unbound motors: $\pi_{\pm} = \pi_0(1 - n_{\pm})$. The detachment rate depends linearly on the fraction of bound motors and exponentially on the carried load [32, 33]: $\epsilon_{\pm} = \epsilon_0 n_{\pm} \exp(\pm F_{\pm}/f_c)$, where f_c

is a critical load above which rapid unbinding occurs. To complete the model with the appropriate geometric feedback, we specify a force-velocity relation for the dyneins [27, 34]: we assume that the motors have a velocity v_0 at zero load that decreases linearly with sliding velocity $\Delta_t \equiv a\phi_t$ and are able to carry a load f_0 when stalled, yielding the expression: $F_{\pm} = \pm f_0(1 \mp \Delta_t/v_0)$.

Motion of the centerline is governed by the classical force balance for an elastic rod in viscous flow [36]: $\partial_s \mathbf{F}_e + \mathbf{f}_v = 0$, where $\mathbf{F}_e(s, t) = \sigma \hat{\mathbf{t}} + N \hat{\mathbf{n}}$ is the elastic force with tension σ and normal force N , and $\mathbf{f}_v(s, t)$ is the viscous force density captured by nonlocal slender body theory [37, 38]. This is accompanied by a moment balance in the z direction: $M_s + N = 0$. Scaling lengths by L , sliding displacement by a , time by the correlation timescale $\tau_0 = 1/(\pi_0 + \epsilon_0)$, elastic forces by B/L^2 , and motor loads by ρf_0 produces four dimensionless groups, of which two are of primary interest: (i) the sperm number $\text{Sp} = L(8\pi\nu/B\tau_0)^{1/4}$, where ν is the viscosity, compares the relaxation time of a bending mode to the motor correlation time; (ii) the activity number $\mu_a = a\rho f_0 L^2/B$ compares motor-induced sliding forces to characteristic elastic forces. The two other dimensionless groups are: $\mu = Ka^2 L^2/B$ and $\zeta = a/(v_0\tau_0)$ [29]. With these scalings, the dimensionless equations for $\phi(s, t)$ read

$$\sigma_{ss} - \left(1 + \frac{c_{\parallel}}{c_{\perp}}\right) N_s \phi_s - N \phi_{ss} - \frac{c_{\parallel}}{c_{\perp}} \sigma \phi_s^2 = c_{\parallel} (\phi_s u_n^d - \partial_s u_t^d), \quad (2)$$

$$N_{ss} - \frac{c_{\perp}}{c_{\parallel}} N \phi_s^2 + \sigma \phi_{ss} + \left(1 + \frac{c_{\perp}}{c_{\parallel}}\right) \sigma_s \phi_s = c_{\perp} (\text{Sp}^4 \phi_t - u_t^d \phi_s - \partial_s u_n^d), \quad (3)$$

$$\phi_{ss} + \mu_a f_m + N = 0, \quad (4)$$

where the first two equations are force balances in the tangential and normal directions while the third is the moment balance. The dimensionless tangential and normal drag coefficients $c_{\parallel, \perp}$ derive from local terms in slender body theory [29] and satisfy $c_{\perp}/c_{\parallel} \rightarrow 2$ for infinitely slender filaments. Hydrodynamic interactions are captured by the disturbance velocity \mathbf{u}^d , with projections u_t^d and u_n^d in the tangential and normal directions, respectively. Given two filaments indexed by $\{\alpha, \beta\}$, the flow is obtained as

$$\mathbf{u}^d(s_{\alpha}) = \mathbf{K}[\mathbf{f}_e^{\alpha}](s_{\alpha}) + \int_0^1 \mathbf{G}(s_{\alpha}; s_{\beta}) \cdot \mathbf{f}_e^{\beta}(s_{\beta}) ds_{\beta}, \quad (5)$$

where $\mathbf{f}_e \equiv \partial_s \mathbf{F}_e$ is the elastic force density. The first term in Eq. (5) is the finite-part integral of slender body theory [29, 37, 38] and captures hydrodynamic interactions within a filament. The second term accounts for the flow induced by the other filament, where the Green's function $\mathbf{G}(s_{\alpha}; s_{\beta})$ is taken to be either the Oseen tensor in free space or Blake's tensor [39] in presence of a no-slip wall.

These equations are supplemented by clamped boundary conditions at $s = 0$, and moment- and force-free conditions at $s = 1$ [29]. In dimensionless form, the evolution equation for the bound motor populations reads

$$\partial_t n_{\pm} = \eta(1 - n_{\pm}) - (1 - \eta)n_{\pm} \exp[f^*(1 \mp \zeta \Delta_t)] + \xi(s, t), \quad (6)$$

where $\eta = \pi_0/(\epsilon_0 + \pi_0)$ is the fraction of time spent by motors in the bound state and $f^* = f_0/f_c$ is the ratio of the stall load to the characteristic unbinding force. The last term accounts for biochemical noise with $\langle \xi(s, t) \rangle = 0$ and $\langle \xi(s, t) \xi(s', t') \rangle = 2\Lambda \delta(s - s') \delta(t - t')$, where Λ is an effective temperature. In the following, we present numerical solutions of the governing equations: Eqs. (2)–(4) are discretized in space using a second-order finite-difference scheme and marched forward with an implicit-explicit method [38], while Eq. (6) for the motor kinetics is integrated using an implicit Euler–Maruyama method.

Spontaneous oscillations.—We first describe the dynamics of isolated filaments, with model parameters estimated from experiments [27–29]. With a choice of $L \sim 50 \mu\text{m}$ for human sperm, $B \sim 0.9 - 1.7 \times 10^{-21} \text{ N m}^2$, $f_0 \sim 1 - 5 \text{ pN}$, $\tau_0 \sim 50 \text{ ms}$ and $\rho \sim 10^3 \mu\text{m}^{-1}$, we estimate $\text{Sp} \sim 8 - 20$ and $\mu_a \sim 2 - 10 \times 10^3$ and explore beating patterns in this range. For a given sperm number, a Hopf bifurcation occurs beyond a critical activity level μ_a^c and gives rise to spontaneous traveling waves reminiscent of sperm waveforms. Close to the bifurcation, the waves propagate from the free end towards the base as previously seen in other simulations of sliding control models [27, 28]. However, far from the bifurcation, nonlinearities give rise to a reversal in the direction of propagation [29], with sperm-like waveforms shown in Fig. 1(b) that resemble experiments [40] and have beating frequencies $f \sim 10 - 15 \text{ Hz}$. In the following discussion, we focus on this anterograde propagation regime as it is biologically most relevant.

Asymmetric beating patterns more typical of cilia can be captured by setting different attachment and detachment rates for the motor populations on \mathbf{x}_{\pm} [29]. This bias in the kinetics allows the flagellum to bend in one direction preferentially, resulting in asymmetric power and recovery strokes as shown in Fig. 1(c). The flagella of wildtype *Chlamydomonas* also have a static mode of deformation [26] that we account for using a spontaneous shape $\phi^0(s)$. To better approximate their asymmetric breaststrokes [Fig. 1(d)], a curvature control mechanism is introduced along with the biased kinetics [29] that uses a generalized Bell's law for the dynein detachment rate: $\epsilon_{\pm} = \epsilon_0 n_{\pm} \exp(F_{\pm}/f_c \pm \kappa(s)/\kappa_c)$, where $\kappa(s)$ is the curvature and κ_c is the threshold value for rapid dissociation. Accounting for the short length $L \sim 6 - 15 \mu\text{m}$ [26] of cilia and *Chlamydomonas* flagella with $B \sim 0.5 - 5 \times 10^{-22} \text{ N m}^2$, we estimate $\text{Sp} \sim 2 - 3$ and measure spontaneous frequencies of $f \sim 10 - 20 \text{ Hz}$.

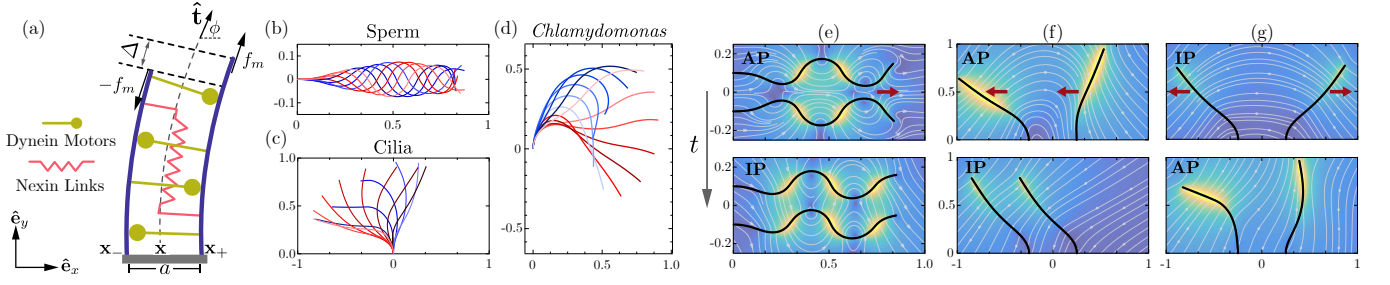


FIG. 1. (a) Schematic representation of the planar model for the flagellar axoneme. (b)–(d) Spontaneous beating patterns emerging from the nonlinear model that approximate the waveforms of sperm, cilia and *Chlamydomonas*. (e)–(g) Synchronization of different beating patterns. The top panel shows snapshots at $t = 0$ and the bottom panel illustrates the final configurations. Sperms (e) beat in phase (IP), while cilia (f)–(g) can achieve both IP or AP synchronization depending on the orientation of the power stroke indicated by red arrows. Synchronization for *Chlamydomonas* (not shown) is identical to that of cilia. See movies showing the temporal dynamics in the Supplemental Material [35].

Pair synchronization.—We first focus on the synchronization of pairs of sperms placed side by side as shown in Fig. 1(e). We initialize the simulation in absence of inter-filament hydrodynamic interactions (HI) by letting spontaneous oscillations reach steady state after saturation of dynein kinetics. The initial configuration is chosen such that the filaments are almost in antiphase (AP) [top panel of Fig. 1(e)]. We then switch on HI and, after several periods, the sperms go in-phase (IP) and remain phase-locked thereafter [bottom panel of Fig. 1(e); see movies in the Supplemental Material [35]]. The key role of hydrodynamics in this process is best illustrated by Fig. 2, showing the evolution of the bound motor populations n_+ at $s = 1/4$ on both filaments (the behavior is identical for n_- and at other locations). Before HI are switched on, motor populations are uncoupled and undergo periodic oscillations in antiphase with cusp-shaped waveforms typical of motors far from equilibrium [41] and only a small fraction of bound motors at any given time. Once HI start acting, both the phase and amplitude of the motor populations change. This is attributed to elastic deformations of the filaments in their induced flow fields, which feed back to the kinetics through the change in sliding displacement and velocity. As seen in Fig. 2,

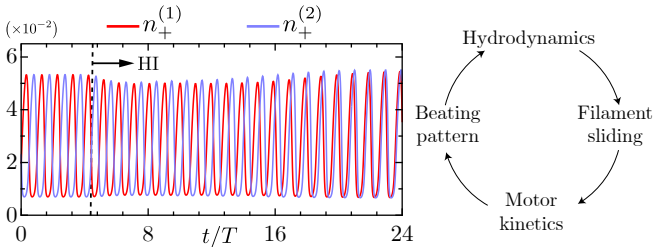


FIG. 2. Evolution of dynein motor populations at $s = 1/4$ on two nearby sperms as a result of HI. The dashed line indicates the instant when interactions are turned on. Time is scaled by the oscillation period T of an isolated filament. Cartoon on the right illustrates the feedback loop leading to synchronization.

the two motor populations rapidly go in phase with a marginally increased amplitude, resulting in spontaneous IP synchronization of the beating patterns. The cartoon in Fig. 2 highlights this cyclic process fundamental to elastohydrodynamic synchronization, by which HI affect beating patterns via geometry dependent motor kinetics. This feedback is most dramatic when the filaments are closely and sufficiently flexible.

A similar mechanism is at play for asymmetric ciliary beats in Fig. 1(f, g). When the power strokes of the two cilia indicated by red arrows point in the same direction, an IP beat emerges with net unidirectional pumping of the fluid [Fig. 1(f)]. When the power strokes are in opposite directions, our model leads to AP synchronization with beating patterns resembling a ‘freestyle’ swimming gait as shown in Fig. 1(g). Similar AP patterns are obtained for *Chlamydomonas* beats, supporting the hypothesis [42] that the IP breaststrokes seen in wildtype cells result from elastic basal couplings between the two flagellar axonemes rather than from HI alone. Indeed, experiments with *vfl* mutants that are deficient in these filamentary connections [42] or with *Volvox* cells held in separate micropipettes [9] have shown AP synchronization for power strokes with opposite orientations, consistent with our model findings.

For a more quantitative analysis of synchronization, we introduce a definition of the phase ψ of a waveform. To this end, we perform the Hilbert transform of the continuous periodic time series $\beta(t) = \phi(1/2, t)$, providing the analytic continuation $\zeta(t) = \beta(t) + i\hat{\beta}(t)$ where $\hat{\beta}(t) \equiv (1/\pi) \int_{-\infty}^{\infty} \beta(\tau)/(t - \tau) d\tau$. The phase of the waveform is then calculated as $\psi(t) = \arctan[\hat{\beta}(t)/\beta(t)]$, and we use an appropriate geometric gauge to define a true phase that grows linearly with time [43]. The phase difference $\delta(t) = \psi_1 - \psi_2$ for two nearby sperms going from AP to IP is shown in Fig. 3(a) and decays to zero over the course of several periods. In spite of the complexity of the governing equations in presence of HI, the phase difference is well described by a simple low-dimensional Adler

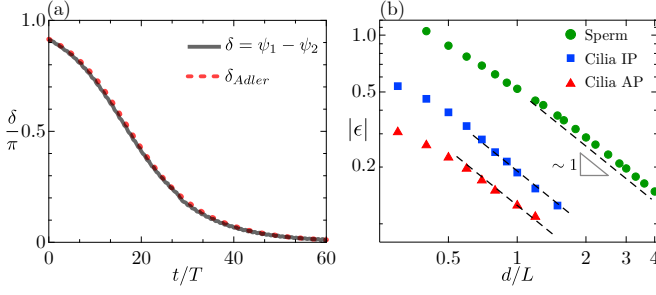


FIG. 3. (a) Evolution of the phase difference $\delta(t)$ during synchronization of two nearby sperms and comparison to the Adler equation (7). (b) Coupling strength $|\epsilon|$ as a function of interflagellar distance d for various beating patterns.

equation as in past experiments with *Chlamydomonas* [6]. Here, we seek a two-parameter equation of the form

$$\dot{\delta} = \epsilon \sin \delta + \alpha \sin 2\delta, \quad (7)$$

where constants ϵ, α are estimated numerically. A solution to this equation follows the numerical data very well in Fig. 3(a). In all our computations, we find that $|\epsilon| \gg |\alpha|$ and thus define $|\epsilon|$ as the effective coupling strength. When plotted as a function of interflagellar distance d in Fig. 3(b), $|\epsilon|$ decays algebraically as $1/d$ in the far field due to dominant Stokeslet HI, with a slower decay at short separations where complex near-field interactions take place. Stronger coupling arises for symmetric spermlike beats than for ciliary beats, primarily due to the longer lengths of sperm flagella. For cilia, we also find that $|\epsilon|_{IP} > |\epsilon|_{AP}$ in agreement with experiments [9], which can be attributed to the fact that filaments spend more time close to one another during IP beats and thus interact more strongly.

Intrinsic to the kinetics of molecular motors is biochemical noise, which alters the precise notion of synchronization. To probe its effects, we study the long-time statistics of the phase difference in presence of noise for spermlike waveforms in Fig. 4(a). Fluctuations follow a Gaussian distribution centered around the mean IP configuration of $\delta = 0$, with a variance scaling linearly with separation distance d . This is a consequence of the $1/d$ decay of the coupling strength $|\epsilon|$ and is further corroborated by the collapse of the distributions under the rescaling $\delta \rightarrow \delta/\sqrt{d}$ in Fig. 4(b) [9]. We model the noisy phase dynamics by a stochastic Adler equation $\dot{\delta} = \epsilon \sin \delta + \chi(t)$ with $\langle \chi(t) \rangle = 0$ and $\langle \chi(t)\chi(t') \rangle = 2D\delta(t-t')$, where D is the phase diffusivity with units of s^{-1} . Associated with the Adler equation is a Fokker-Planck description for the probability distribution $P(\delta)$ of the phase difference, with steady-state solution given by $P(\delta) = \exp(-\epsilon \cos \delta/D)/2\pi I_0(|\epsilon|/D)$, where I_0 is the modified Bessel function of order zero and where we estimate D numerically [29, 44]. The interaction potential $U(\delta) = -\ln P(\delta)$, which is 2π -periodic, is shown in Fig. 4(d) for increasing noise levels. When noise is weak, the

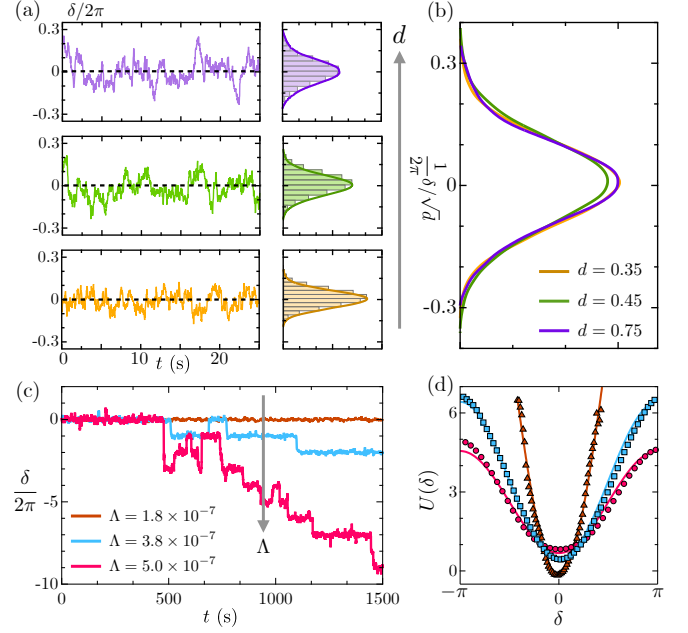


FIG. 4. (a) Gaussian distributions of the fluctuations of the phase difference for varying separation distance d . (b) Collapse of the distributions in the rescaled variable δ/\sqrt{d} . (c) Long-time evolution of $\delta(t)$ for increasing biochemical noise Λ at a fixed separation distance d , showing the emergence of slips. (d) Effective interaction potential $U(\delta)$ estimated from the statistics (symbols) and compared to the Fokker-Planck prediction (lines).

filaments remain phase-locked and fluctuate around the IP configuration, which translates into a deep potential well at $\delta = 0$. With increasing noise, the potential well flattens as deviations from perfect AP synchrony become more frequent and intense. Occasionally, accumulated noise allows the filaments to gather a complete phase of 2π , causing them to ‘slip’ towards $\delta \pm 2\pi$. These slips are visible in the phase trajectories of Fig. 4(c) and can be interpreted as thermally assisted hops between neighboring wells in the flattened periodic potential. In absence of frequency mismatch, slips are equally probable in $\pm 2\pi$, and the stochastic Adler model predicts a frequency of $G = D|I_0(|\epsilon|/D)|^{-2}/4\pi^2$ [44]. With the computed value of D , this yields $G = 0.0035 s^{-1}$ for the case $\Lambda = 5 \times 10^{-7}$ in Fig. 4(c), which is in good agreement with the measured frequency of $G = 0.0042 s^{-1}$.

Concluding remarks.—Using a detailed microscopic model of the flagellar axoneme that produces spontaneous oscillations similar to those seen in nature, we have illuminated the role of hydrodynamic interactions and associated mechanochemical feedback in enabling synchronization of nearby flagella and cilia. Our model predictions for various beating patterns and orientations all agree with experiments and give credence to the sliding control mechanism responsible for the spontaneous beats. While we have focused on interactions in free space, our simulations suggest that the qualitative behavior is unal-

tered in presence of no-slip walls albeit with weaker coupling strengths due to the additional viscous damping. We were also able to reproduce experimentally observed phase slips induced by biochemical noise. Future studies with our model will probe the role of elastic basal couplings [42], swimming sperms that are free to adjust phase by sliding past one another [45], and emergent dynamics in large-scale ciliary arrays.

* Email address: dstn@ucsd.edu

- [1] V. Rothschild, *Nature* **163**, 358 (1949).
- [2] G. I. Taylor, *Proc. R. Soc. Lond. A* **209**, 447 (1951).
- [3] R. Golestanian, J. M. Yeomans, and N. Uchida, *Soft Matter* **7**, 3074 (2011).
- [4] U. R  tger and W. N  ltsch, *Cell Motility* **5**, 251 (1985).
- [5] M. Polin, I. Tuval, K. Drescher, J. P. Gollub, and R. E. Goldstein, *Science* **325**, 487 (2009).
- [6] R. E. Goldstein, M. Polin, and I. Tuval, *Phys. Rev. Lett.* **103**, 168103 (2009).
- [7] K. C. Leptos, K. Y. Wan, M. Polin, I. Tuval, A. I. Pesci, and R. E. Goldstein, *Phys. Rev. Lett.* **111**, 158101 (2013).
- [8] K. Y. Wan, K. C. Leptos, and R. E. Goldstein, *J. R. Soc. Interface* **11**, 20131160 (2014).
- [9] D. R. Brumley, K. Y. Wan, M. Polin, and R. E. Goldstein, *eLife* **3**, e02750 (2014).
- [10] A. Pikovsky, M. Rosenblum, J. Kurths, and J. Kurths, *Synchronization: A Universal Concept in Nonlinear Sciences* (Cambridge University Press, 2003).
- [11] A. Vilfan and F. J  licher, *Phys. Rev. Lett.* **96**, 058102 (2006).
- [12] T. Niedermayer, B. Eckhardt, and P. Lenz, *Chaos* **18**, 037128 (2008).
- [13] N. Uchida and R. Golestanian, *Phys. Rev. Lett.* **106**, 058104 (2011).
- [14] A. Maestro, N. Bruot, J. Kotar, N. Uchida, R. Golestanian, and P. Cicuta, *Commun. Phys.* **1**, 28 (2018).
- [15] S. Gueron, K. Levit-Gurevich, N. Liron, and J. J. Blum, *Proc. Natl. Acad. Sci. USA* **94**, 6001 (1997).
- [16] J. Elgeti and G. Gompper, *Proc. Natl. Acad. Sci. USA* **110**, 4470 (2013).
- [17] H. Guo, L. Fauci, M. Shelley, and E. Kanso, *J. Fluid Mech.* **836**, 304 (2018).
- [18] R. E. Goldstein, E. Lauga, A. I. Pesci, and M. R. Proctor, *Phys. Rev. Fluids* **1**, 073201 (2016).
- [19] P. Bayly and S. Dutcher, *J. R. Soc. Interface* **13**, 20160523 (2016).
- [20] G. De Canio, E. Lauga, and R. E. Goldstein, *J. R. Soc. Interface* **14**, 20170491 (2017).
- [21] F. Ling, H. Guo, and E. Kanso, *J. R. Soc. Interface* **15**, 20180594 (2018).
- [22] J. Han and C. S. Peskin, *Proc. Natl. Acad. Sci. USA* **115**, 4417 (2018).
- [23] C. B. Lindemann, *J. Theor. Biol.* **168**, 175 (1994).
- [24] C. J. Brokaw, *J. Exp. Biol.* **55**, 289 (1971).
- [25] P. V. Bayly and K. S. Wilson, *Biophys. J.* **107**, 1756 (2014).
- [26] P. Sartori, V. F. Geyer, A. Scholich, F. J  licher, and J. Howard, *eLife* **5**, e13258 (2016).
- [27] D. Oriola, H. Gad  lha, and J. Casademunt, *Royal Soc. Open Sci.* **4**, 160698 (2017).
- [28] I. H. Riedel-Kruse, A. Hilfinger, J. Howard, and F. J  licher, *HFSP J.* **1**, 192 (2007).
- [29] B. Chakrabarti and D. Saintillan, *Phys. Rev. Fluids* **4**, 043102 (2019).
- [30] S. Camalet and F. J  licher, *New J. Phys.* **2**, 24 (2000).
- [31] O. du Roure, A. Lindner, E. Nazockdast, and M. J. Shelley, *Annu. Rev. Fluid Mech.* **51**, 539 (2019).
- [32] K. Svoboda and S. M. Block, *Cell* **77**, 773 (1994).
- [33] M. J. I. M  ller, S. Klumpp, and R. Lipowsky, *Proc. Natl. Acad. Sci.* **105**, 4609 (2008).
- [34] M. J. Shelley, *Annu. Rev. Fluid Mech.* **48**, 487 (2016).
- [35] See Supplemental Material at [URL will be inserted by publisher] for various movies showing temporal dynamics of synchronization.
- [36] S. S. Antman, *Nonlinear Problems of Elasticity* (Springer, 1995).
- [37] J. Keller and S. Rubinow, *J. Fluid Mech.* **75**, 705 (1976).
- [38] A.-K. Tornberg and M. J. Shelley, *J. Comput. Phys.* **196**, 8 (2004).
- [39] J. R. Blake, *Math. Proc. Cambridge Phil. Soc.* **70**, 303 (1971).
- [40] C. Brokaw, *J. Exp. Biol.* **43**, 155 (1965).
- [41] F. J  licher and J. Prost, *Phys. Rev. Lett.* **75**, 2618 (1995).
- [42] K. Y. Wan and R. E. Goldstein, *Proc. Natl. Acad. Sci. USA* **113**, E2784 (2016).
- [43] B. Kralemann, L. Cimponeriu, M. Rosenblum, A. Pikovsky, and R. Mrowka, *Phys. Rev. E* **77**, 066205 (2008).
- [44] R. L. Stratonovich, *Topics in the Theory of Random Noise* (CRC Press, 1967).
- [45] Y. Yang, J. Elgeti, and G. Gompper, *Phys. Rev. E* **78**, 061903 (2008).